Inverse Problems and Imaging
Volume 2, No. 2, 2008, 1–XX

Web site: http://www.aimSciences.org

ENHANCED IMAGING FROM MULTIPLY SCATTERED WAVES

Romina Gaburro and Clifford J Nolan

Department of Mathematics and Statistics, University of Limerick
Castletroy, Limerick, Ireland

(Communicated by Margaret Cheney)

Abstract. Many imaging methods involve probing a material with a wave and observing the back-scattered wave. The back-scattered wave measurements are used to compute an image of the internal structure of the material. Many of the conventional methods make the assumption that the wave has scattered just once from the region to be imaged before returning to the sensor to be recorded. The purpose of this paper is to show how this restriction can be partially removed and also how its removal leads to an enhanced image, free of the artifacts often associated with the conventionally reconstructed image.

1. **Introduction.** In many inverse problems and imaging modalities, one seeks to recover internal properties of an object from remote measurements. A good example of this is Synthetic Aperture Radar (SAR), which is a very successful imaging technique in which a plane or satellite carrying an antenna moves along a flight track. The antenna emits pulses of electromagnetic radiation, which scatter off the terrain and the scattered waves are detected with the same antenna. The received signals are then used to produce an image of the terrain (see [4], [12], [13], [14]).

A similar procedure is used for Synthetic Aperture Sonar, using an array of transducers instead of an antenna; here the goal is to map the seafloor. Synthetic Aperture focusing techniques are also used in non-destructive evaluation such as ultrasonic medical imaging, where high-frequency acoustic energy is transmitted into the human body using a set of transducers (see [7], [9]). Another very popular application of these kinds of techniques is in geophysics (see [1], [2], [3], [11], [16]).

The nature of the imaging problem depends on the directivity of the antenna. Here we are interested in the case where the antenna has poor directivity and a typical example of that is the foliage-penetrating RADAR (see [12], [20], [21]), whose low frequencies do not allow for much beam focusing.

We consider the case when a single pass is made over the scene, so that backscattered data is known for sensor positions along a curve (a straight line in our case). The data depend on two variables, namely the (fast) time variable and the position of the antenna along the flight track (slow variable). Because the data depend on two degrees of freedom, we expect to be able to reconstruct a two-dimensional image of the scene. We assume that the target to be imaged is located on the ground, which has known topography and that it is also near a perfectly reflective vertical wall. This will improve the traditional backprojection imaging methods.

2000 *Mathematics Subject Classification.* Primary: 35S30; Secondary: 35L05.
Key words and phrases. SAR, multiple scattering, microlocal analysis.
The authors are supported by Science Foundation Ireland grant 03/IN3/I401.

This problem has been considered in [15] where the case of a focused beam is treated. In the presence of the aforementioned wall, the emitted wave has four different ways it can scatter before returning to be recorded. These correspond to the different paths that the wave can take when scattering to and from the ground. For example the wave may scatter directly to and from the ground or it may first scatter from the wall and then off the ground, etc. We will refer to these different scattering paths as "experiments" throughout the paper. In [15] the authors analyse the case when individual data due to different experiments can be isolated from the full data collected; the reconstruction of the image can be done there separately by back-projecting any individual data set. The present paper differs from [15] as we use the theory of microlocal analysis to explain how the imaging works, how artifacts arise, and how they may be eliminated. Moreover, in this work the RADAR is assumed to be operating with a poor directivity, so the beam forming of the wave is not applicable in this situation, where the receiver and source antenna beam patterns coincide. This implies that different experiments will interfere with each other (see [15]).

The high-frequency deviation of the speed of wave propagation from that in air is known as the ground reflectivity function. The forward scattering operator (by definition) maps the reflectivity function to the scattered waves that are recorded by the same emitting antenna (i.e., the antenna acts as a source and receiver). A weak-scattering approximation is used here which makes the forward scattering operator a linear one. Moreover the operator is a Fourier Integral Operator (FIO) (see [6], [8], [15], [19]). Such operators map singular distributions to other singular distributions and the relationship between the input and the output singularities forms what is called a canonical relation. Canonical relations associated to FIOs are Lagrangian manifolds and have a rich geometric structure (see [6], [14]). The authors study this in detail for the case of RADAR.

The paper is organized as follows. In Section 2 we briefly recall the mathematical model for the scattering operator in the presence of a vertical wall. This model is obtained via the method of images (see [15] for more details). Section 3 is devoted to the analysis of the scattering operator and its canonical relation. The forward operator is a sum of four forward operators (see [15]) to which four canonical relations are associated. These correspond to the different paths that the wave can take when scattering to and from the ground. To obtain an image, we must back-project the data which means applying a sum of four adjoint scattering operators to the data. This leads to sixteen possible contributions to the image. There is a lot of symmetry and we are able to analyse the resulting image. We show that it is possible to have artifacts in the image and we indicate the relationship between the true scatterer and the artifact. We also quantify how narrow a beam is required (if beam forming is possible) in order to avoid such artifacts. Our analysis focuses on the case where the antenna is moving at a fixed height along a straight line perpendicular to the vertical wall. The choice of this particular flight path affords a simple enough setting to be able to analyse the imaging process completely and concretely. Moreover, we show that similar results can be obtained when the antenna is flying on a straight line at a fixed height and making a small angle with the perpendicular to the wall. This shows our results are stable with respect to the direction of the flight track.

In the case of a flight path which is not close to being perpendicular to the wall, the analysis becomes much more awkward. However, we illustrate that the

qualitative nature of the artifacts is unchanged for such non-perpendicular flight path.
We conclude the paper with two appendices and some conclusions. In Appendix 1 we give a technical calculation needed in Section 3, while Appendix 2 is devoted to some further analysis of the composition of the canonical relations.

2. **The mathematical model of scattering.** We consider the simple scalar wave equation to model the wave propagation

$$\left(\nabla^2 - \frac{1}{c^2(x)}\,\partial_t^2\right)U(t,x) = f, \tag{2.1}$$

where U is the wave field, f describes the source, and the function c is the wave propagation speed. Although the correct model is Maxwell's equations, 2.1 is commonly used in SAR and represents a good model for sonar and ultrasound for example. As in [15] we make the following assumptions.

Assumption 1. We assume that the target is well separated from the region where the sensors are located and that in the intervening region $c(x) = c_0$, where c_0 is the (assumed constant) speed of light in air.

Assumption 2. We assume that the target to be imaged is a-priori known to lie on the ground and lies strictly on one (known) side of a vertical wall. We assume that the ground is locally flat, so if we denote by (x_1, x_2, x_3) the cartesian coordinates in $\mathbb{R}^3$, then the ground can be locally identified with the plane $\{(x_1,\, x_2,\, 0) \mid x_i \in \mathbb{R},\, i = 1,\, 2\} \subseteq \mathbb{R}^3$.

The vertical wall can be taken for simplicity as the infinite vertical plane $x_1 = 0$ so we can identify the area to be imaged by the set $\mathbb{R}^2_+ = \{(x_1,\, x_2,\, 0) \mid x_i \in \mathbb{R},\, i = 1,\, 2,\, x_1 > 0\}$.

We write the total field U as the sum

$$U = U^{in} + U^{sc},$$

where U^{in} and U^{sc} represent the incoming field emanated from the antenna (or source array) and the scattered field respectively. We denote by

$$\Gamma_+ := \left\{\mathbf{\Gamma}_+(s) \;\mid\; s^{min} < s < s^{max}\right\}$$

the curve describing the antenna flight track, i.e. $\Gamma_+(s)$ is the source (antenna) location, for any $s \in (s^{min},\, s^{max})$. Let us also define for any $s \in (s^{min},\, s^{max})$, $\Gamma_-(s)$ as the mirror image of $\Gamma_+(s)$ with respect to the plane $x_1 = 0$. We will say that $\Gamma_+(s)$, $\Gamma_-(s)$ are the real and the virtual source respectively, for any $s \in (s^{min},\, s^{max})$.

There are four ways for the wave to hit the target on the ground and return to the antenna. Indeed the wave may scatter directly to and from the target. Or, the wave may scatter first from the wall, then from the target and finally back to the antenna. The third means of scattering is the reverse of the former and finally, the last method involves scattering from the wall on the way down to the target and again from the wall on the way back to the antenna. See Figure 2 for an illustration of this.

In [15], the following (readily interpretable) expression for the scattered wave field $d(s,\, t)$ collected at antenna position $\Gamma_+(s)$, at time t has been derived

$$
\begin{aligned}
d(s,\, t) = & \int e^{-i\omega\left(t-2|x-\Gamma_+(s)|/c_0\right)}\, a_1(x,\, s,\, t,\, \omega)\, V(x)\, d\omega\, dx \\
& - 2\int e^{-i\omega\left(t-(|x-\Gamma_+(s)|+|x-\Gamma_-(s)|)/c_0\right)}\, a_2(x,\, s,\, t,\, \omega)\, V(x)\, d\omega\, dx \\
& + \int e^{-i\omega\left(t-2|x-\Gamma_-(s)|/c_0\right)}\, a_4(x,\, s,\, t,\, \omega)\, V(x)\, d\omega\, dx,
\end{aligned} \tag{2.2}
$$

where $V(x) = \frac{1}{c_0^2} - \frac{1}{c^2(x)}$ is the *reflectivity function*. The reflectivity function encodes rapid changes in material properties. For example, when the radio wave impinges on a building on the ground, the propagation speed changes suddenly, according to the building materials. The second line of 2.2 incorporates two symmetric situations, the first being the one where the wave bounces off the wall and scatters on the ground to go back to the source, the second being the other way around. The amplitudes involved in these two experiments are a_2 and a_3 respectively but $a_2 = a_3$ in the case when the receiver and source antenna beam patterns coincide (see [15]). The amplitudes $a_i, i = 1, \dots 4$ are geometrical optics amplitudes, and encode the geometrical spreading, beam pattern, etc, for the emitted and measured waves. The phases in 2.2 are readily identifiable with the travel times associated with the four different experiments. These four different situations are illustrated in Figure 2. More detail on this is given later in this paper. We wish to reconstruct the function V from the data d, i.e., solve an inverse problem.

Statement of the inverse problem: The idealized inverse problem consists in determining V from the knowledge of $d(s,\, t)$, for any $(s,\, t) \in [s^{min},\, s^{max}] \times [0,\, T]$, for some T.

2.1. **The scattering operator.** We follow the idea of [15] in representing the (perfectly reflecting) wall via the method of images, by placing a virtual source $\Gamma_-(s)$ symmetrically on the other side of the wall from the actual source $\Gamma_+(s)$. Note that the argument s in $\Gamma_\pm(s)$ denotes the current real and virtual source position respectively, as it is moved over a path parametrized by s.

The data that is collected contains all four kinds of scattering events in it. The amplitudes a_i, $1 \le i \le 4$ in 2.2 are given by the following expressions (see [15])

$$
\begin{aligned}
a_1(x,\, s,\, t,\, \omega) &= \frac{\omega^2\, p(\omega)\, j_s^2\big(\omega(\widehat{x-\Gamma_+(s)}),\, \Gamma_+(s)\big)\, m(s,\, t)}{(4\pi)^2\, |\, x-\Gamma_+(s)\, |^2}, \\
a_2(x,\, s,\, t,\, \omega) &= a_3(x,\, s,\, t,\, \omega) \\
&= \frac{\omega^2\, p(\omega)\, j_s\big(\omega(\widehat{x-\Gamma_+(s)}),\Gamma_+(s)\big) j_s\big(\omega(\widehat{x-\Gamma_-(s)}),\Gamma_-(s)\big)\, m(s,\, t)}{(4\pi)^2\, |\, x-\Gamma_+(s)\, |\, |\, x-\Gamma_-(s)\, |}, \\
a_4(x,\, s,\, t,\, \omega) &= \frac{\omega^2\, p(\omega)\, j_s^2\big(\omega(\widehat{x-\Gamma_-(s)}),\, \Gamma_-(s)\big)\, m(s,\, t)}{(4\pi)^2\, |\, x-\Gamma_-(s)\, |^2},
\end{aligned}
$$

where j_s and $p(\omega)$ are terms due to the fact that in the real scenario the antenna is not a point source $\delta(x)$ and the signal sent to the antenna is not a delta function $\delta(t)$. In fact, j_s is related to the current density distribution over the antenna,

and $p(\omega)$ is the Fourier transform of waveform $P(t)$ sent to the antenna (see [10]). Finally $m(s,\, t)$ is a *mute* used to avoid artifacts that would occur due to the fact that we abruptly cut off the signal at the start and end of the flight track and also at the start and end of the recording time interval:

$$m \in C_0^\infty([s^{min},\, s^{max}] \times [0,\, T]).$$

For technical reasons, we need to assume

Assumption 3. For $1 \le j \le 4$, the amplitude a_j satisfies

$$\sup_{(s,\, t,\, x) \in K} |\, \partial_\omega^\alpha\, \partial_s^\beta\, \partial_t^\delta\, \partial_x^\rho\, a_j(x,\, s,\, t,\, \omega)\, | \le C^j_{K,\, \alpha,\, \beta,\, \delta,\, \rho}(1+\omega^2)^{(2-|\alpha|)/2}, \tag{2.3}$$

where K is any compact set in $[s_{min}, s_{max}] \times [0,T] \times \mathbb{R}^2_+$ and α, β, δ, ρ are arbitrary multi-indices of the appropriate dimension.

The above assumption is valid for example when the waveform P is approximately a delta function and the antenna is sufficiently broadband (see [1], [13]).

Definition 2.1. We denote the scattering region $\mathbb{R}^2_+$ by $\mathcal{X}$ and the data space $(s^{min},\, s^{max}) \times [0,\, T]$ by $\mathcal{Y}$.

We denote the *scattering operator* from scene V to data d given by 2.2 by F so that

$$\begin{aligned} FV(s,\, t) = &\int e^{-i\omega\left(t - 2|x-\Gamma_+(s)|/c_0\right)}\, a_1(x,\, s,\, t,\, \omega)\, V(x)\, d\omega\, dx \\ &- 2\int e^{-i\omega\left(t - (|x-\Gamma_+(s)| + |x-\Gamma_-(s)|)/c_0\right)}\, a_2(x,\, s,\, t,\, \omega)\, V(x)\, d\omega\, dx \\ &+ \int e^{-i\omega\left(t - 2|x-\Gamma_-(s)|/c_0\right)}\, a_4(x,\, s,\, t,\, \omega)\, V(x)\, d\omega\, dx \\ &:= F_1\, V(s,\, t) + F_2\, V(s,\, t) + F_3\, V(s,\, t) + F_4\, V(s,\, t), \end{aligned} \tag{2.4}$$

where $F_2 = F_3$. Assumption 3 implies that the forward operators $F_j, 1 \le j \le 4$ are Fourier integral operators (FIOs) [15].

3. Analysis of the scattering operator.

We start this section by recalling some arguments regarding FIOs. We saw in Section 2 that $F_i, 1 \le i \le 4$ is a FIO and standard arguments in FIO theory give us information about how $F_i, 1 \le i \le 4$ maps singularities from the scene into the data. We will review this below, and to begin with, we recall the following

Definition 3.1. Let $\mathcal{X}$, $\mathcal{Y}$ be as in Definition 2.1, $\mathcal{E}'(\mathcal{X})$, $\mathcal{E}'(\mathcal{Y})$ be the spaces of distrubutions with compact support in $\mathcal{X}$ and $\mathcal{Y}$ respectively. If F is a Fourier Integral Operator

$$F : \mathcal{E}'(\mathcal{X}) \longrightarrow \mathcal{E}'(\mathcal{Y})$$

given by the oscillatory integral

$$Fu(y) = \int e^{i\phi(y,\, x,\, \omega)}\, a(y,\, x,\, \omega)\, u(x)\, d\omega\, dx, \tag{3.1}$$

for any $u \in \mathcal{E}'(\mathcal{X})$, then its (twisted) **canonical relation** is the set

$$\begin{aligned}\Lambda'_F = &\Big\{\big((y,\,\eta),\,(x,\,\xi)\big) \in T^\star(\mathcal{Y}\times\mathcal{X})\setminus\{0\} \;\mid\; (y,\,x,\,\omega)\in C_\phi \cap \mathrm{EssSupp}(a),\\ &\eta = D_y\phi(y,\,x,\,\omega),\,\xi = -D_x\phi(y,\,x,\,\omega)\Big\},\end{aligned} \tag{3.2}$$

where D_x and D_y denote the gradients with respect to the x and y variable respectively and $\{0\}$ is the zero section of $T^*(\mathcal{X}\times\mathcal{Y})$. The set C_ϕ is defined as the critical set points

$$C_\phi = \big\{(y,\,x,\,\omega) \;\mid\; D_\omega\phi(y,\,x,\,\omega) = 0\big\}, \tag{3.3}$$

which is called the **critical manifold**, and EssSupp(a) is defined via its complement:

$$\begin{aligned}{}^{\mathcal{C}}\mathrm{EssSupp}(a) = &\{(y,\,x,\,\omega) \;\mid\; a(y,x,\omega) \text{ and its derivatives decrease faster}\\ &\text{than any negative power of } \omega, \text{ as } \mid\omega\mid\to\infty\}.\end{aligned}$$

Note that the frequency ω can be multi-dimensional.

Definition 3.2. If we denote by $\mathcal{D}'(\mathcal{X})$ the set of distributions on $\mathcal{X}$ and if $u \in \mathcal{D}'(\mathcal{X})$, then the **wave front set WF(u)** of u is defined as the complement in $T^\star\mathcal{X}\setminus\{0\}$ of the collection of all $(x,\,\xi) \in T^\star\mathcal{X}\setminus\{0\}$ such that there exists a neighborhood U of x and a neighborhood $\mathcal{U}$ of ξ such that for any $\varphi \in C_0^\infty(U)$, with $x \in supp(\varphi)$ and any $N \in \mathbb{N}$:

$$\mathcal{F}(\varphi\,u)(\tau\xi) = O(\tau^{-N}), \qquad \text{for} \quad \tau\to\infty, \quad \text{uniformly in} \quad \xi\in\mathcal{U}.$$

Here $\mathcal{F}(\varphi\,u)$ denotes the Fourier transform of $\varphi\,u$.

Remark 1. WF(u) is a closed cone in $T^\star\mathcal{X}\setminus\{0\}$ and its singular support satisfies $\mathrm{singsupp}(u) = \pi\big(WF(u)\big)$, where π is the natural projection of $T^\star\mathcal{X}\setminus\{0\}$ into $\mathcal{X}$ (see [6]).

Definition 3.3. If F is given by 3.1 with distributional kernel $K_F \in \mathcal{D}'(\mathcal{Y}\times\mathcal{X})$ given by the oscillatory integral

$$K_F(y,\,x) = \int e^{i\phi(y,\,x,\,\omega)}a(y,\,x,\,\omega)\,d\omega,$$

the **wavefront relation WF′(F)** is defined by

$$WF'(F) = \Big\{\big((y,\,\eta),\,(x,\,\xi)\big) \in T^\star(\mathcal{Y}\times\mathcal{X})\setminus\{0\} \mid (y,\,x,\,\eta,\,-\xi) \in WF(K_F)\Big\}.$$

It turns out (see [6]) that

$$\begin{aligned}WF(Fu) &\subseteq WF'(F)\circ WF(u)\\ WF'(F) &\subseteq \Lambda'_F,\end{aligned} \tag{3.4}$$

where"$\circ$" stands for the following composition

$$WF'(F)\circ WF(u) = \{\ (y,\eta)\mid \exists\ ((y,\eta),(x,\xi)) \in WF'(F)\ \}. \tag{3.5}$$

Let us compute the canonical relations $\Lambda'_{F_i}, 1 \le i \le 4$. Note that $\Lambda'_{F_2} = \Lambda'_{F_3}$, so we will only compute $\Lambda'_{F_i}, i = 1, 2, 4$.

$$
\begin{aligned}
\Lambda'_{F_1} = \Big\{ & \big((s,\, t,\, \sigma,\, \tau),\, (x,\, \xi)\big) \mid\ t = 2\ \mid x - \Gamma_+(s) \mid /c_0; \\
& \sigma = 2\tau(x - \widehat{\Gamma_+}(s)) \cdot \dot{\Gamma}_+(s)/c_0; \\
& \tau = -\omega; \\
& \xi = -2\tau(x - \widehat{\Gamma_+}(s))/c_0 \Big\};
\end{aligned}
\tag{3.6}
$$

$$
\begin{aligned}
\Lambda'_{F_2} = \Big\{ & \big((s,\, t,\, \sigma,\, \tau),\, (x,\, \xi)\big) \mid\ t = \big(\ \mid x - \Gamma_+(s) \mid + \mid x - \Gamma_-(s) \mid\ \big)/c_0; \\
& \sigma = \tau\Big((x - \widehat{\Gamma_+}(s)) \cdot \dot{\Gamma}_+(s) + (x - \widehat{\Gamma_-}(s)) \cdot \dot{\Gamma}_-(s)\Big)/c_0; \\
& \tau = -\omega; \\
& \xi = -\tau\Big((x - \widehat{\Gamma_+}(s)) + (x - \widehat{\Gamma_-}(s))\Big)/c_0 \Big\};
\end{aligned}
\tag{3.7}
$$

$$
\begin{aligned}
\Lambda'_{F_4} = \Big\{ & \big((s,\, t,\, \sigma,\, \tau),\, (x,\, \xi)\big) \mid\ t = 2\ \mid x - \Gamma_-(s) \mid /c_0; \\
& \sigma = 2\tau(x - \widehat{\Gamma_-}(s)) \cdot \dot{\Gamma}_-(s)/c_0; \\
& \tau = -\omega; \\
& \xi = -2\tau(x - \widehat{\Gamma_-}(s))/c_0 \Big\},
\end{aligned}
\tag{3.8}
$$

where $\dot{\Gamma}$ denotes the derivative of Γ with respect to s. The forward map is given by the four contributions

$$F = F_1 + F_2 + F_3 + F_4$$

and the adjoint of F, $F^\star$ by

$$F^\star = F_1^\star + F_2^\star + F_3^\star + F_4^\star,$$

where $F_i^\star$ is the adjoint of F_i. Singularities in the scene will be mapped into singularities in the data by any of the F_i, while singularities in the data will be mapped into singularities in the scene by the adjoint maps $F_i^\star$.

Forming an image usually involves operating on the data with a weighted adjoint operator (the reason for this will become clear soon).

Our goal is to analyse the resulting image, determine which kind of artifacts it may contain, and see if we can avoid them. To do so we need to analyse the composition of the (twisted) canonical relations

$$\Lambda'_{F_i^\star} \circ \Lambda'_{F_j}, \qquad \text{for any} \quad 1 \le i, j \le 4, \tag{3.9}$$

where

$$\Lambda'_{F_i^\star} = {}^t\Lambda'_{F_i}, \qquad \text{for any} \quad 1 \le i \le 4,$$

and the superscript t denotes the transposed relation.

The reason for this is that if we denote by I the reconstructed image, FIO theory implies

$$\begin{aligned} WF(I) &\subseteq WF'(F^\star) \circ WF'(F) \circ WF(V) \\ &\subseteq \left(\bigcup_{i,j=1}^{4} \Lambda_i'^\star \circ \Lambda_j' \right) \circ WF(V). \end{aligned} \tag{3.10}$$

The compositions in 3.9 and 3.10 are meant as compositions of relations, i.e. if $\mathcal{R}_1 \subset U \times V$, $\mathcal{R}_2 \subset V \times W$ are relations, then the *composition* $\mathcal{R}_1 \circ \mathcal{R}_2 \subset U \times W$ is defined by

$$\mathcal{R}_1 \circ \mathcal{R}_2 = \big\{(u,w) \in U \times W;\ \exists v \in V : (u,v) \in \mathcal{R}_1 \text{ and } (v,w) \in \mathcal{R}_2\big\}.$$

For any $i,\ j = 1, \dots, 4$, we will sometimes refer in the sequel to *case* or *pair* $(i,\ j)$ or speak about *interaction between experiments* i *and* j by meaning we are analysing the object $\Lambda'_{F_i^\star} \circ \Lambda'_{F_j}$ (or similarly $\Lambda'_{F_j^\star} \circ \Lambda'_{F_i}$).

3.1. **Perpendicular trajectory case.**

3.1.1. *Analysis of the diagonal terms.* We need only analyse $\Lambda'_{F_2^\star} \circ \Lambda'_{F_2}$ (pair (2, 2)) among the diagonal compositions in 3.9 as pair (1, 1) (and similarly (4, 4)) have been studied in [12], while case (3, 3) is very similar to (2, 2). Let us denote by $x = (x_1, x_2, 0)$ a point on the ground. By recalling 3.7 we have

$$\sigma = \tau\Big((x - \widehat{\Gamma_+(s)}) \cdot \dot\Gamma_+(s) + (x - \widehat{\Gamma_-(s)}) \cdot \dot\Gamma_-(s) \Big)/c_0 \tag{3.11}$$

$$t = \big(\ |\ x - \Gamma_+(s)\ |\ +\ |\ x - \Gamma_-(s)\ |\ \big)/c_0. \tag{3.12}$$

In RADAR terminology, equations 3.11 and 3.12 define the so called iso-doppler and iso-range contours of a bistatic SAR scenario, respectively (see [17], [22]). For sake of simplicity we make the following assumption.

Assumption 4. The antenna is flying perpendicular to the wall $x_1 = 0$ at constant height h, i.e.

$$\begin{aligned} \Gamma_+(s) &= (\gamma_1(s),\ 0,\ h) = (\gamma_1,\ 0,\ h) \\ \Gamma_-(s) &= (-\gamma_1(s),\ 0,\ h) = (-\gamma_1,\ 0,\ h), \end{aligned}$$

so that with arc length as the parametrization, the real and the virtual velocity fields are as follows

$$\begin{aligned} \dot\Gamma_+(s) &:= V_+ = (1,\ 0,\ 0) \\ \dot\Gamma_-(s) &:= V_- = (-1,\ 0,\ 0). \end{aligned}$$

With appropriate time units, we may take $c_0 = 1$. Define

$$R_+ := \big[(x_1 - \gamma_1)^2 + x_2^2 + h^2\big]^{1/2} = |\ x - \Gamma_+(s)\ | \tag{3.13}$$

$$R_- := \big[(x_1 + \gamma_1)^2 + x_2^2 + h^2\big]^{1/2} = |\ x - \Gamma_-(s)\ | \tag{3.14}$$

$$p := \frac{\sigma}{\tau}, \tag{3.15}$$

so that 3.11, 3.12 become

$$\frac{x_1-\gamma_1}{R_+}-\frac{x_1+\gamma_1}{R_-}=p \tag{3.16}$$

$$R_+ + R_- = t. \tag{3.17}$$

Notice that the travel time condition given by 3.17 tells us that for any s and t the iso-range contours are located at the intersection of the ellipsoid of revolution (whose foci are $\Gamma_+(s)$ and $\Gamma_-(s)$) with the earth's surface. In our specific case where the earth is locally flat, this intersection is an ellipse. The equation of this ellipse can be obtained by squaring 3.17 a couple of times and rearranging to get

$$x_2^2=\Big(\frac{t^2}{4}-\gamma_1^2-h^2\Big)+\Big(\frac{4\gamma_1^2}{t^2}-1\Big)x_1^2. \tag{3.18}$$

Notice that 3.18 defines an ellipse if $t>2\gamma_1$ and $t^2-(2\gamma_1)^2-(2h)^2>0$. In a realistic SAR scenario, these conditions are fulfilled during the measurements of the scattered field.
One can directly verify the identity

$$4\gamma_1 x_1 = R_-^2 - R_+^2 \tag{3.19}$$

and by substituting $R_- = t-R_+$ in the latter equation and rearranging it we obtain

$$x_1=\frac{t}{4\gamma_1}\big(t-2R_+\big). \tag{3.20}$$

Substituting 3.20 into 3.16, we obtain the following quadratic equation for R_+

$$R_+^2 - tR_+ + \frac{\alpha}{4} = 0, \tag{3.21}$$

with

$$\alpha=\frac{t(t^2-4\gamma_1^2)}{(t+p\gamma_1)}, \tag{3.22}$$

giving two possible solutions

$$R_+=\frac{t\pm(t^2-\alpha)^{1/2}}{2},$$

but $R_+ < t/2$, which leaves the unique solution

$$R_+=\frac{t-(t^2-\alpha)^{1/2}}{2}. \tag{3.23}$$

By 3.23 and 3.20 we finally get

$$x_1=\frac{t(t^2-\alpha)^{1/2}}{4\gamma_1}, \tag{3.24}$$

so that x_1 is uniquely determined. Since we are operating the RADAR in side-scan mode, x_2 is uniquely determined (no sign ambiguity) by (3.18), and since $x_3=0$ for a scatterer on the ground, we have that the scatterer location x is determined. This shows that there are no artifacts present in the image obtained from experiment 2.

Remark 2.

$$0<\alpha<t^2. \tag{3.25}$$

The latter inequality is needed for a real root in (3.24) and we prove it in Appendix 1.

3.1.2. *Analysis of the non-diagonal terms.* We analyse the relations $\Lambda'_{F_i^*} \circ \Lambda'_{F_j}$ for $i \neq j$ in this subsection. Again we assume that the antenna is flying perpendicularly to the wall i.e. Assumption 4 holds. In that case we have

$$\begin{aligned} \sigma_1 &= \frac{2\tau}{c_0}\,\frac{x_1-\gamma_1}{R_+} \\ \sigma_2 = \sigma_3 &= \frac{\tau}{c_0}\left(\frac{x_1-\gamma_1}{R_+} - \frac{x_1+\gamma_1}{R_-}\right) \\ \sigma_4 &= -\frac{2\tau}{c_0}\,\frac{x_1+\gamma_1}{R_-}. \end{aligned} \tag{3.26}$$

Notice that

$$\sigma_1\,|_{x_1=0} = \sigma_2\,|_{x_1=0} = \sigma_3\,|_{x_1=0} = \sigma_4\,|_{x_1=0} = -\frac{2\tau}{c_0}\,\frac{\gamma_1}{R_+\,|_{x_1=0}} < 0$$

and

$$\lim_{x_1\to\infty}\sigma_1(x) = \frac{2\tau}{c_0}; \quad \lim_{x_1\to\infty}\sigma_2(x) = \lim_{x_1\to\infty}\sigma_3(x) = 0; \quad \lim_{x_1\to\infty}\sigma_4(x) = -\frac{2\tau}{c_0}.$$

Moreover

$$\begin{aligned} \partial_{x_1} R_+ &= R_+^{-1}(x_1-\gamma_1) \\ \partial_{x_1} R_- &= R_-^{-1}(x_1+\gamma_1) \end{aligned} \tag{3.27}$$

and

$$\begin{aligned} \partial_{x_1}\sigma_1 &= \frac{2\tau}{c_0}\,\frac{R_+ - (x_1-\gamma_1)\partial_{x_1}R_+}{R_+^2} \\ &= \frac{2\tau}{c_0}\,\frac{R_+^2-(x_1-\gamma_1)^2}{R_+^3} \\ \partial_{x_1}\sigma_2 = \partial_{x_1}\sigma_3 &= \frac{\tau}{c_0}\left\{\frac{R_+ - (x_1-\gamma_1)\partial_{x_1}R_+}{R_+^2} - \frac{R_+^2-(x_1-\gamma_1)^2}{R_+^3}\right\} \\ &= \frac{\tau}{c_0}\,\frac{(x_2^2+h^2)(R_-^3-R_+^3)}{(R_+R_-)^3} \\ \partial_{x_1}\sigma_4 &= \frac{2\tau}{c_0}\,\frac{R_- - (x_1-\gamma_1)\partial_{x_1}R_-}{R_-^2} \\ &= -\frac{2\tau}{c_0}\,\frac{R_-^2-(x_1+\gamma_1)^2}{R_-^3}. \end{aligned} \tag{3.28}$$

By 3.13, 3.14 we have that $R_+ > (x_1-\gamma_1)$ and $R_- > (x_1+\gamma_1)$, which imply that $\partial_{x_1}\sigma_1 > 0$ and $\partial_{x_1}\sigma_4 < 0$, respectively, i.e. σ_1 is increasing and σ_4 is decreasing in the x_1-direction. Moreover $R_- > R_+ > 0$ as the target is located on the right hand side of the vertical wall $x_1 = 0$, which implies that $\partial_{x_1}\sigma_2 > 0$,

$\partial_{x_1}\sigma_3 > 0$, i.e. σ_2, σ_3 are increasing in the x_1-direction. Therefore, it's impossible to get a common value between σ_1 and σ_4 and between σ_2 or σ_3 and σ_4. We can therefore conclude that the composition in 3.9 is empty for the pairs $(i,j) = (1,4),(4,1),(2,4),(4,2),(3,4),(4,3)$ (see Figures 6 and 7).

Let us consider pairs $(i,j) = (1,2),(2,1)$. Cases $(i,j) = (1,3),(3,1)$ can be treated in a similar way. We assume again that Assumption 4 holds and we denote by $x = (x_1, x_2, 0)$ and $z = (z_1, z_2, 0)$ two points on the ground. In order to compose $\Lambda_{F_1^*} \circ \Lambda_{F_2}$ (or similarly $\Lambda_{F_2^*} \circ \Lambda_{F_1}$) at points x, z we must have (for coincidence of σ values)

$$2\,\frac{z_1-\gamma_1}{R^z_+} = \left(\frac{x_1-\gamma_1}{R^x_+} - \frac{x_1+\gamma_1}{R^x_-}\right), \tag{3.29}$$

moreover x, z must satisfy the two travel time conditions respectively

$$R^x_+ + R^x_- = t \tag{3.30}$$

$$2R^z_+ = t, \tag{3.31}$$

where we have used the notation R^x_+ for R_+ defined in (3.13) for the scattering point x and R^z_+ when the scattering point x is replaced by z, etc.

By combining 3.29, 3.30 and 3.31 we obtain

$$t(t-R^x_+)(x_1-\gamma_1) - tR^x_+(x_1+\gamma_1) = 4R^x_+(t-R^x_+)(z_1-\gamma_1), \tag{3.32}$$

from which we extract the following expression for z_1 as a function of x

$$z_1 = \Big[\big(4(R^x_+)^2 + t^2 - 4tR^x_+\big)\gamma_1 + \big(2tR^x_+ - t^2\big)x_1\Big]/4((R^x_+)^2 - tR^x_+). \tag{3.33}$$

Using equations (3.21) and (3.23), it follows that

$$z_1 = \left(\frac{t^2-\alpha}{4\gamma_1\alpha}\right)\,\left(t^2-4\gamma_1^2\right), \tag{3.34}$$

which in turn implies that

$$z_1 - x_1 = \left[(t^2-\alpha)(t^2-4\gamma_1^2)/\alpha - t(t^2-\alpha)^1/2\right]/\alpha. \tag{3.35}$$

Note that α (defined in (3.22)) is a function of p, which is a function of x_1. Therefore, (3.35) gives us a formula for the distance between z_1 and x_1 in terms of x_1. It follows that if we want to avoid artifacts resulting from back-projecting with (possibly weighted) operators $F_i^*, i = 1,2$, we must ensure that the beam width in the first coordinate direction is smaller than that predicted by the right hand side of (3.35). Note that this implies a variable beam width restriction, which depends on the (x_1) location that is being illuminated for imaging. This beam forming can be done synthetically and it therefore does not impose extra logistical difficulties in acquiring the data.

If the required beam forming is not possible, then artifacts will be present in the scene and their location can be predicted by intersecting the line given by (3.35) for any fixed x_1, with the circle given by the intersection between the sphere (3.31) and the earth. Of course, this may not be a complete determination if the usual left-right ambiguity of RADAR is still present (due to not being able to operate in

side-scan mode).

Figures 9, 10, 11 show the intersection of the iso-range and iso-doppler contours of F_1, F_2 (or F_3) and F_4 respectively.

3.2. **Non-perpendicular case.** Let us suppose the antenna is flying along a straight line at a fixed height h, at an angle θ to the vertical to the wall, and define

$$k = \tan\theta. \tag{3.36}$$

For any $x = (x_1, x_2, 0)$, we also define the usual range quantities

$$R^x_+ := \left[(x_1-\gamma_1)^2 + (x_2 - k\gamma_1)^2 + h^2\right]^{1/2} = \mid x - \Gamma_+(s) \mid \tag{3.37}$$

$$R^x_- := \left[(x_1+\gamma_1)^2 + (x_2 - k\gamma_1)^2 + h^2\right]^{1/2} = \mid x - \Gamma_-(s) \mid . \tag{3.38}$$

3.2.1. *Analysis of the diagonal terms.* In this case equations 3.16, 3.17 are replaced by

$$\begin{aligned} &\frac{x_1-\gamma_1+kx_2-k^2\gamma_1}{R^x_+} - \frac{x_1+\gamma_1-kx_2+k^2\gamma_1}{R^x_-} = p \\ &R^x_+ + R^x_- \;=\; t \end{aligned} \tag{3.39}$$

respectively. For a fixed value of p, we define

$$\begin{aligned} F_1(k;x_1,x_2) &:= \frac{x_1-\gamma_1+kx_2-k^2\gamma_1}{R^x_+} - \frac{x_1+\gamma_1-kx_2+k^2\gamma_1}{R^x_-} - p \\ F_2(k;x_1,x_2) &:= R^x_+ + R^x_- - t. \end{aligned}$$

For $k = 0$ we have

$$\begin{aligned} \frac{\partial F_1}{\partial x_1}(0;x_1,x_2) &= \frac{(R^x_+)^2-(x_1-\gamma_1)^2}{(R^x_+)^3} - \frac{(R^x_-)^2-(x_1+\gamma_1)^2}{(R^x_-)^3} \\ &= \frac{(x_2^2+h^2)\big((R^x_-)^3-(R^x_+)^3\big)}{(R^x_+R^x_-)^3} \\ \frac{\partial F_1}{\partial x_2}(0;x_1,x_2) &= x_2\frac{(R^x_+)^3(x_1+\gamma_1)-(R^x_-)^3(x_1-\gamma_1)}{(R^x_+R^x_-)^3} \\ \frac{\partial F_2}{\partial x_1}(0;x_1,x_2) &= \frac{x_1-\gamma_1}{R^P_+} + \frac{x_1+\gamma_1}{R^x_-} \\ &= \frac{R^x_-(x_1-\gamma_1)+R^x_+(x_1+\gamma_1)}{R^x_+R^x_-} \\ \frac{\partial F_2}{\partial x_2}(0;x_1,x_2) &= \frac{x_2}{R^x_+} + \frac{x_2}{R^x_-} \\ &= x_2\frac{R^x_- + R^x_+}{R^x_+R^x_-}. \end{aligned}$$

If $F : \mathbb{R}\times\mathbb{R}^2 \longrightarrow \mathbb{R}^2$ is the map defined by

$$F(k;x_1,x_2) := \Big(F_1(k;x_1,x_2),\; F_2(k;x_1,x_2)\Big)$$

and we compute the jacobian of F at $(0; x_1, x_2)$,

$$\big|F'(0;x_1,x_2)\big| = \left|\left(\frac{\partial F_1}{\partial x_1}\frac{\partial F_2}{\partial x_2} - \frac{\partial F_1}{\partial x_2}\frac{\partial F_2}{\partial x_1}\right)(0;x_1,x_2)\right|, \tag{3.40}$$

we obtain

$$\big|F'(0;x_1,x_2)\big| = \frac{x_2}{(R_+^x R_-^x)^4}\, J(0;x_1,x_2), \tag{3.41}$$

where

$$\begin{aligned} J(0;x_1,x_2) &= (R_+^x R_-^x)(x_2^2+h^2)\big((R_-^x)^3 - (R_+^x)^3\big)\big) \\ &-\big[R_-^x(x_1-\gamma_1) + R_+^x(x_1+\gamma_1)\big]\big[(R_+^x)^3(x_1+\gamma_1)(R_-^x)^3(x_1-\gamma_1)\big]. \end{aligned} \tag{3.42}$$

It is possible to give a proof that J does not vanish at points away from the wall in certain situations. Rather than do this we instead give a plot of J as a function of x_1 (see figure 1), which clearly demonstrates that it is a strictly monotonic function and vanishes only at $x_1 = 0$.

By the Implicit Function Theorem, for any point $x = (x_1, x_2, 0)$ satisfying

$$F_1(0;x_1,x_2) = 0 \tag{3.43}$$

$$F_2(0;x_1,x_2) = 0 \tag{3.44}$$

and $J(0;x_1,x_2) \neq 0, x_2 \neq 0$, there exists a neighborhood U of 0, neighborhoods V_1, V_2 of x_1, x_2 in $\mathbb{R}$ respectively and two unique functions $g_1 : U \to V_1$, $g_2 : U \to V_2$, with $g_1, g_2 \in C^1(U)$ such that

$$F\big(k; g_1(k), g_2(k)\big) = 0. \tag{3.45}$$

We can therefore conclude that the behavior of artifacts for small angles θ is similar to case above where $\theta = 0$.

3.2.2. *Analysis of the non-diagonal terms.* We start by considering the interaction between experiment 1 and 2, i.e., the $(1,2)$ case (the case $(1,3)$ can be treated similarly). Following the same argument of Section 3.2.1 we define for any $x = (x_1,\ x_2,\ 0)$, $z = (z_1,\ z_2,\ 0)$

$$F_1(k;x_1,x_2,z_1,z_2) := \frac{z_1 - \gamma_1 + kz_2 - k^2\gamma_1}{R_+^z} \tag{3.46}$$

$$F_2(k;x_1,x_2,z_1,z_2) := 2\, R_+^z \tag{3.47}$$

$$F_3(k;x_1,x_2,z_1,z_2) := \frac{x_1 - \gamma_1 + kx_2 - k^2\gamma_1}{R_+^x} - \frac{x_1 + \gamma_1 - kx_2 + k^2\gamma_1}{R_-^x} \tag{3.48}$$

$$F_4(k;x_1,x_2,z_1,z_2) := R_+^x + R_-^x. \tag{3.49}$$

Let us consider the map $F : \mathbb{R} \times \mathbb{R}^4 \longrightarrow \mathbb{R}^4$ defined by

$$F(k;x_1,x_2,z_1,z_2) = \Big(F_1, F_2, F_3, F_4\Big)(x_1,x_2,z_1,z_2),$$

whose Jacobian with respect to the last four variables valuated at $k = 0$ is given by

$$\left|F'(0;x_1,x_2,z_1,z_2)\right| = \begin{vmatrix} 0 & 0 & \frac{R^z_+-(z_1-\gamma_1)^2}{(R^z_+)^3} & -\frac{z_2(z_1-\gamma_1)}{(R^z_+)^3} \\ 0 & 0 & 2\,\frac{z_1-\gamma_1}{R^z_+} & 2\,\frac{z_2}{R^z_+} \\ L_1 & L_2 & 0 & 0 \\ L_3 & L_4 & 0 & 0 \end{vmatrix},$$

where

$$L_1 = \frac{\partial F_3}{\partial x_1} = \frac{(x_2^2+h^2)\big((R^x_-)^3-(R^x_+)^3\big)}{(R^x_+R^x_-)^3} \tag{3.50}$$

$$L_2 = \frac{\partial F_3}{\partial x_2} = x_2\,\frac{(R^x_+)^3(x_1+\gamma_1)-(R^x_-)^3(x_1-\gamma_1)}{(R^x_+R^x_-)^3} \tag{3.51}$$

$$L_3 = \frac{\partial F_4}{\partial x_1} = \frac{R^x_-(x_1-\gamma_1)+R^x_+(x_1+\gamma_1)}{R^x_+R^x_-} \tag{3.52}$$

$$L_4 = \frac{\partial F_4}{\partial x_2} = x_2\,\frac{R^P_-+R^x_+}{R^x_+R^x_-} \tag{3.53}$$

and

$$\begin{vmatrix} L_1 & L_2 \\ L_3 & L_4 \end{vmatrix} = \frac{x_2}{(R^x_+R^x_-)^4}\,J(0;x_1,x_2),$$

where $J(0;x_1,x_2)$ is explicitly given by 3.42. Then we obtain

$$\left|F'(0;x_1,x_2,z_1,z_2)\right| = \frac{2z_2}{(R^z_+)^3}\,\frac{x_2}{(R^x_+R^x_-)^4}\,J(0;x_1,x_2). \tag{3.54}$$

Like for case (2, 2), if one stays away from imaging the axis $x_2=0, x_3=0$, then the quantity to check for non-vanishing is $J(0;x_1,x_2)$.

We proceed by considering the pair (2, 4) (or similarly (3, 4)). Expressions 3.46-3.49 are replaced by the following

$$F_1(k;x_1,x_2,z_1,z_2) := \frac{z_1+\gamma_1-kz_2+k^2\gamma_1}{R^z_+} \tag{3.55}$$

$$F_2(k;x_1,x_2,z_1,z_2) := 2\,R^z_- \tag{3.56}$$

$$F_3(k;x_1,x_2,z_1,z_2) := \frac{x_1-\gamma_1+kx_2-k^2\gamma_1}{R^x_+} - \frac{x_1+\gamma_1-kx_2+k^2\gamma_1}{R^x_-} \tag{3.57}$$

$$F_4(k;x_1,x_2,z_1,z_2) := R^x_+ + R^x_- \tag{3.58}$$

and if $F : \mathbb{R}\times\mathbb{R}^4 \longrightarrow \mathbb{R}^4$ is the map with components F_i, $i=1,\dots,4$ given by 3.55-3.58, then its Jacobian with respect to the last four variables, evaluated at $k=0$ is given by

$$\left|F'(0;x_1,x_2,z_1,z_2)\right| = \begin{vmatrix} 0 & 0 & \frac{(R^z_-)^2-(z_1+\gamma_1)^2}{(R^z_-)^3} & -\frac{z_2(z_1+\gamma_1)}{(R^z_-)^3} \\ 0 & 0 & 2\,\frac{z_1+\gamma_1}{R^z_-} & 2\,\frac{z_2}{R^z_-} \\ L_1 & L_2 & 0 & 0 \\ L_3 & L_4 & 0 & 0 \end{vmatrix},$$

where $L_1, \ldots, L_4$ are given by 3.50 – 3.53. By computing the above determinant we get

$$\left|F'(0; x_1, x_2, z_1, z_2)\right| = \frac{2z_2}{(R^z_-)^3}\,\frac{x_2}{(R^x_+ R^x_-)^4}\,J(0; x_1, x_2), \tag{3.59}$$

where $J(0; x_1, x_2)$ is explicitly given by 3.42. 3.59 is very similar to 3.54 with R^z_+ being replaced by R^z_-.

We finally analyse case (1, 4). 3.46-3.49 are replaced by

$$F_1(k; x_1, x_2, z_1, z_2) := \frac{z_1 - \gamma_1 + kz_2 - k^2\gamma_1}{R^z_+} \tag{3.60}$$

$$F_2(k; x_1, x_2, z_1, z_2) := 2\,R^z_+ \tag{3.61}$$

$$F_3(k; x_1, x_2, z_1, z_2) := \frac{x_1 + \gamma_1 - kx_2 + k^2\gamma_1}{R^x_-} \tag{3.62}$$

$$F_4(k; x_1, x_2, z_1, z_2) := 2\,R^x_- \tag{3.63}$$

and if $F : \mathbb{R}\times\mathbb{R}^4 \longrightarrow \mathbb{R}^4$ is the map with components F_i, $i = 1, \ldots, 4$ given by 3.60-3.63, then its Jacobian with respect to the last four variables evaluated at $k = 0$ is given by

$$\left|F'(0; x_1, x_2, z_1, z_2)\right| = \begin{vmatrix} 0 & 0 & \frac{(R^z_-)^2-(z_1-\gamma_1)^2}{(R^z_+)^3} & -\frac{z_2(z_1-\gamma_1)}{(R^z_+)^3} \\ 0 & 0 & 2\,\frac{z_1-\gamma_1}{R^z_+} & 2\,\frac{z_2}{R^z_+} \\ \frac{(R^x_-)^2-(z_1+\gamma_1)^2}{(R^z_-)^3} & -\frac{x_2(x_1+\gamma_1)}{(R^x_-)^3} & 0 & 0 \\ 2\,\frac{x_1+\gamma_1}{R^x_-} & 2\,\frac{x_2}{R^x_-} & 0 & 0 \end{vmatrix},$$

which gives us

$$\left|F'(0; x_1, x_2, z_1, z_2)\right| = \frac{4x_2\,z_2}{(R^z_+)^2\,(R^x_-)^2}, \tag{3.64}$$

which never vanishes as along as one stays away from the axis $x_2 = 0$, $x_3 = 0$. This completes our study of stability of our imaging results for flight tracks that are not too far from being perpendicular to the wall.

4. **Conclusions.** In this study we have provided a theoretical supplement to [15]. We focused our analysis on the case where the source/receiver is moving at a fixed height, along a straight line perpendicular to the wall. Such a particular case provides a simplification in the analytical study of the problem and a better understanding on how artifacts arise in the scene and how they can be avoided if operating the RADAR in side-scan mode (see Fig 3, Fig 4 and Fig 5 for example).

We have also shown that similar results to those obtained in the perpendicular case hold for small deviation of the trajectory of the antenna from the perpendicular one too. This proves that our results are stable with respect to the direction of the flight track.

For large deviations from the perpendicular trajectory, such as for example 45^0, similar results to those found in this work can be shown numerically (Fig 12, Fig 13 below illustrate how artifacts produced in this setting are qualitatively of the same

kind as those introduced in the perpendicular case). Figures 14 and 15 show the intersections between the iso-range and iso-doppler contours of F_1 and F_2 (or F_3) in this situation (a similar picture to the one obtained in Fig 14 for F_1 can be found for F_4). We notice that the iso-doppler contours in Fig 14 and Fig 15 look very similar to the rotation of 45^0 of the iso-doppler contours obtained for the perpendicular case (Fig 9 and Fig 10 respectively) and this similarity is quite evident for the case of F_1.

Appendix 1.

Proof of Remark 2. We start by proving the right hand side inequality of 3.25 and in order to do so, we show that

$$\frac{t^2 - 4\gamma_1^2}{t + p\gamma_1} < t. \tag{4.1}$$

As a first step we prove that ($c_0 = 1$)

$$pt > -4\gamma_1. \tag{4.2}$$

Let us suppose by contradiction that 4.2 does not hold, i.e. $pt \leq -4\gamma_1$, then by 3.17 we get

$$p(R_+ + R_-) \leq -4\gamma_1.$$

If we recall 3.16 and define $\beta = \gamma_1^2 + x_2^2 + h^2$ we obtain

$$\beta - x_1^2 \geq R_+ R_-. \tag{4.3}$$

By definition of R_+, R_- we have

$$(R_+ R_-)^2 = x_1^4 + 2\beta x_1^2 - 4x_1^2\gamma_1^2 + \gamma_1^2, \tag{4.4}$$

then 4.3, 4.4 together imply

$$4\gamma_1^2 x_1^2 \leq x_1^2\gamma_1^2,$$

i.e.

$$\beta \leq \gamma_1^2, \tag{4.5}$$

which is a contradiction due to the definition of β, and so we have

$$t + p\gamma_1 > \frac{t^2 - 4\gamma_1^2}{t}, \tag{4.6}$$

which proves that $\alpha < t^2$. Moreover notice that 4.6 together with the triangle inequality $2\gamma_1 < t$ proves also that $\alpha > 0$ and this concludes the proof. □

Appendix 2. Let us consider pair $(1, 4)$. We have shown in Section 3.1.2 that there is no interaction between experiments 1 and 4 (when forming a back-projected image) for the case where the antenna is flying perpendicularly to the wall. In Section 3.2.2 we proved that there is no interaction between these two experiments also for the case when the antenna is flying at a fixed high h, on a straight line, in a direction such that the angle between the velocity field and the perpendicular to the wall is small enough.

We consider here the general case where the antenna is flying at a fixed high h but in a general direction i.e. on a straight line forming a general angle from the perpendicular to the wall.

We recall that the travel time conditions and the σ-conditions are

$$t_1 = 2 \mid x - \Gamma_+(s) \mid /c_0; \tag{4.7}$$

$$\sigma_1 = 2\tau(\widehat{x - \Gamma_+(s)}) \cdot \dot{\Gamma}_+(s)/c_0; \tag{4.8}$$

for experiment 1 at the point $x = (x_1,\, x_2,\, 0)$ and

$$t_4 = 2 \mid z - \Gamma_-(s) \mid /c_0; \tag{4.9}$$

$$\sigma_4 = 2\tau(\widehat{z - \Gamma_-(s)}) \cdot \dot{\Gamma}_-(s)/c_0; \tag{4.10}$$

at $z = (z_1,\, z_2,\, 0)$ for experiment 4. If h is the constant height at which the antenna is flying, then the real and virtual source can be written in coordinates as

$$\Gamma_+(s) = (\gamma_1(s),\, \gamma_2(s),\, h) = (\gamma_1,\, \gamma_2,\, h)$$
$$\Gamma_-(s) = (-\gamma_1(s),\, \gamma_2(s),\, h) = (-\gamma_1,\, \gamma_2,\, h),$$

and the real and the virtual velocity fields as

$$\dot{\Gamma}_+(s) := V_+ = (v_1,\, v_2,\, 0)$$
$$\dot{\Gamma}_-(s) := V_- = (-v_1,\, v_2,\, 0).$$

By equating σ_1 and σ_4 we get

$$\frac{(x_1 - \gamma_1)v_1 + (x_2 - \gamma_2)v_2}{\mid x - \Gamma_+(s) \mid} = \frac{(z_1 + \gamma_1)(-v_1) + (z_2 - \gamma_2)v_2}{\mid z - \Gamma_-(s) \mid} \tag{4.11}$$

and recalling that another condition for the existence of the composite map $\Lambda'_{F_1^\star} \circ \Lambda'_{F_4}$ (or $\Lambda'_{F_4^\star} \circ \Lambda'_{F_1}$) at x, z is $t_1 = t_4$, we have

$$\mid x - \Gamma_+(s) \mid = \mid z - \Gamma_-(s) \mid . \tag{4.12}$$

If we combine 4.11 and 4.12 we obtain

$$x_1 v_1 + x_2 v_2 = z_2 v_2 - z_1 v_1, \tag{4.13}$$

which can be written in the form

$$\begin{bmatrix} x_1 + z_1 \\ x_2 - z_2 \end{bmatrix} \cdot \begin{bmatrix} v_1 \\ v_2 \end{bmatrix} = 0.$$

If the antenna is not flying perpendicularly to the wall i.e. $v_2 \neq 0$, then for any point $z = (z_1, z_2, 0)$ on the circle 4.9, equation 4.13 represents the line through the reflected point $\tilde{z} = (-z_1, z_2, 0)$ of z with respect to the x_2-axis and slop $-v_1/v_2$. By intersecting this line with circle 4.7, we get a point $x = (x_1, x_2, 0)$ for which

$$t_1 = |\, x - \Gamma_+(s) \,| = |\, z - \Gamma_-(s) \,| = t_4; \tag{4.14}$$

$$\sigma_1 = (\widehat{x - \Gamma_+(s)}) \cdot \dot{\Gamma}_+(s) = (\widehat{z - \Gamma_-(s)}) \cdot \dot{\Gamma}_-(s) = \sigma_4 \tag{4.15}$$

and conclude that x, z are the real scatterer and the artifact (or viceversa) when forming the back-projected image given by pair (1, 4) or (4, 1) (see Figure 16).

This kind of artifacts arising in the image are partially avoided by illuminating only one side of the wall and partially by operating in side-scan mode.

When the antenna is flying perpendicularly to the wall, then 4.13 is simply replaced by

$$x_1 = -z_1, \tag{4.16}$$

and a similar argument stated for the case when $v_2 \neq 0$ can then be adopted to the case $v_2 = 0$ as well.

5. **Figures.**

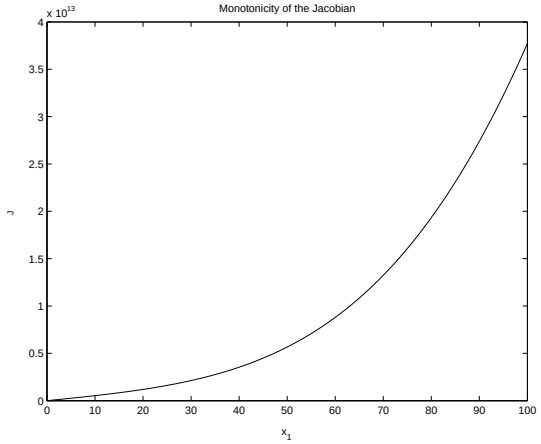

FIGURE 1. The above graph of J vs x_1 has the following fixed parameters $x_2 = 10$, $\Gamma_1(s) = 20$, $\Gamma_2 = 0$, $h = 50$. One can clearly see that it only vanishes at $x_1 = 0$ and in fact that it is a monotonic increasing function of x_1.

Acknowledgments. RG and CN acknowledge the support of Science Foundation Ireland (Grant 03/IN3/I401).

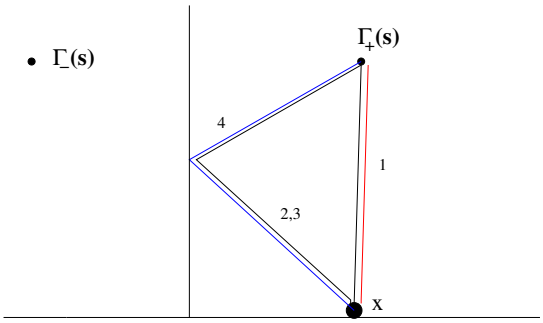

FIGURE 2. In experiment 1, the wave scatters directly to and from the target. In experiments 2, the wave scatters from the wall to the target and back to the receiver. In experiment 3, the wave scatters from the target to the wall and back to the receiver. Finally, in experiment 4, the wave scatters to the wall to the target and back to the wall again before returning to the receiver.

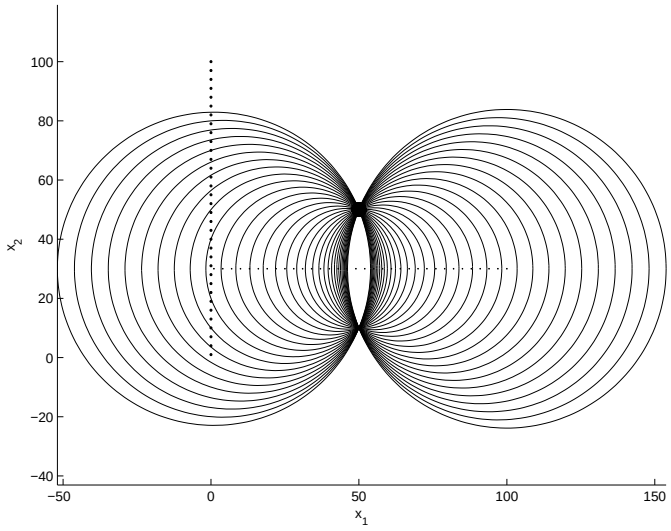

FIGURE 3. Picture showing the iso-range contours of F_1: the spheres with centre along the flight track intersect at the scatterer (50, 50) and at the artifact location. The antenna is moving perpendicularly to the wall, at a fixed height $h = 30$. The vertical and horizontal lines on the figure represent the wall and the flight track respectively.

REFERENCES

[1] G. Beylkin, *Imaging of discontinuities in the inverse scattering problem by inversion of a causal generalized Radon transform*, J. Math. Phys., **26** (1985), no.1, 99–108, MR:0776132.

[2] G. Beylkin and R. Burridge, *Linearized inverse scattering problems in acoustic and elasticity*, Wave Motion, **12** (1990), no.1, 15–52, MR1033486.

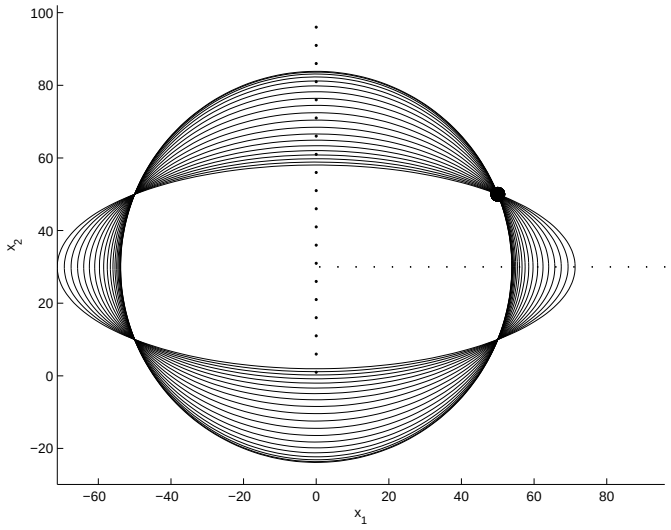

FIGURE 4. Picture showing the iso-range contours of $F_2 = F_3$ in the same setting as in Fig 3: the ellipsoids with foci along the flight track intersect at the scatterer $(50, 50)$ and at the artifact locations.

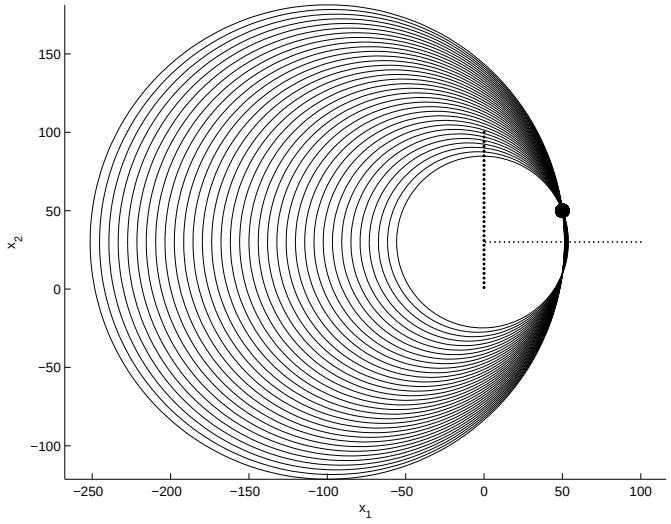

FIGURE 5. Picture showing the iso-range contours of F_4 in the same setting as in Fig 3, 4: the spheres centred at the virtual source intersect at the scatterer $(50, 50)$ and at the artifact location.

[3] N. Bleistein, J. K. Cohen and J. W. Stockwell, "The Matematics of Multidimensional Seismic Inversion," Springer-Verlag, New York, 2000.

[4] M. Cheney, *A mathematical tutorial on synthetic aperture radar*, SIAM Review, **43** (2001), no.2, 301–312, MR:1861084.

[5] M. Cheney and R. J. Bonneau, *Imaging that exploits multipath scattering from point scatterers*, Inverse Problems, **20** (2004), no.5, 1691–1711, MR2109144.

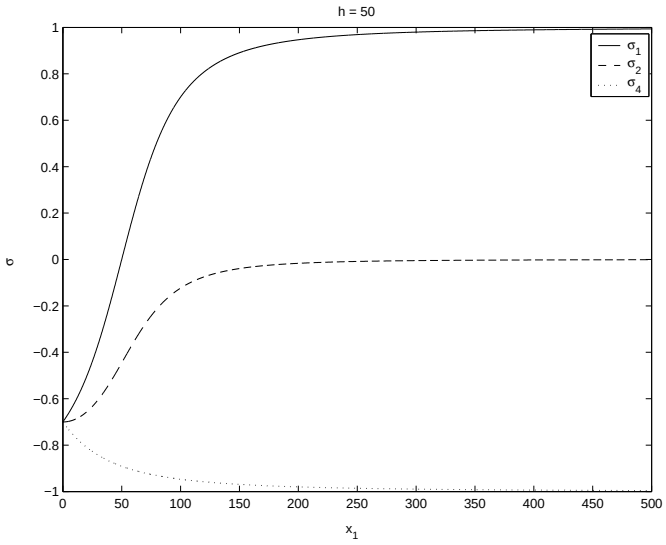

FIGURE 6. Figure shows the graph of σ_1, σ_2 and σ_4 when the antenna is flying on a straight line perpendicular to the wall, at the fixed height of $h = 50$ and the source location is $\Gamma_+ = (50, 10, 50)$.

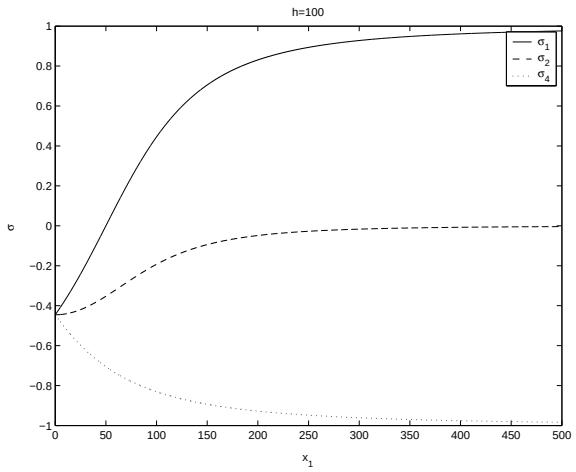

FIGURE 7. Figure shows the graph of σ_1, σ_2 and σ_4 when the antenna is flying on a straight line perpendicular to the wall, at the fixed height of $h = 100$ and the source location is $\Gamma_+ = (50, 10, 100)$.

[6] J. J. Duistermaat, "Fourier Integral Operators. Progress in Mathematics, 130, " Birkhauser, Boston, 1996, MR:1362544.
[7] R. Gaburro, C. J. Nolan, T. Dowling and M. Cheney, *Imaging from multiply scattered waves*, Proc. SPIE 6513, 651304 (2007).

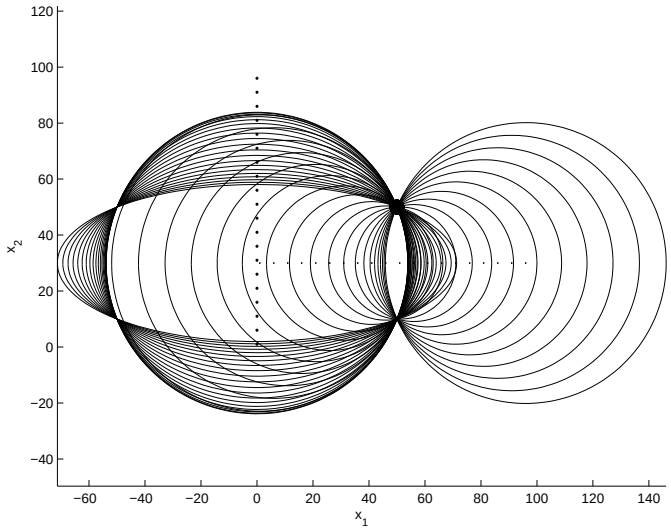

FIGURE 8. Picture showing the iso-range contours of F_1 and F_2 contributing to the back-projection $\Lambda_{F_1^*} \circ \Lambda_{F_2}$: the spheres, centred at the real source moving along the flight track, intersect the ellipsoids, with foci along the flight track, at the scatterer (50, 50) and at the artifact locations. Here the antenna is moving perpendicularly to the wall at a fixed height $h = 30$.

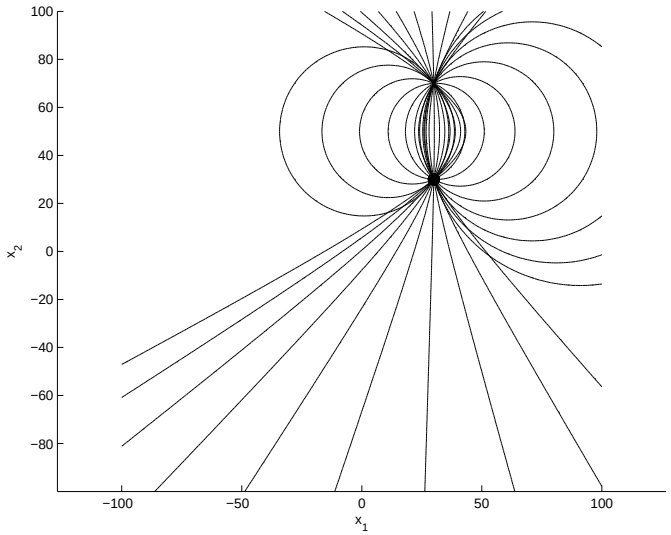

FIGURE 9. Figure shows intersections of the iso-range and iso-doppler contours of F_1 at the scatterer (30, 30) and at the artifact location, in the case when the antenna is flying on a straight line perpendicular to the wall, at the fixed height of $h = 25$.

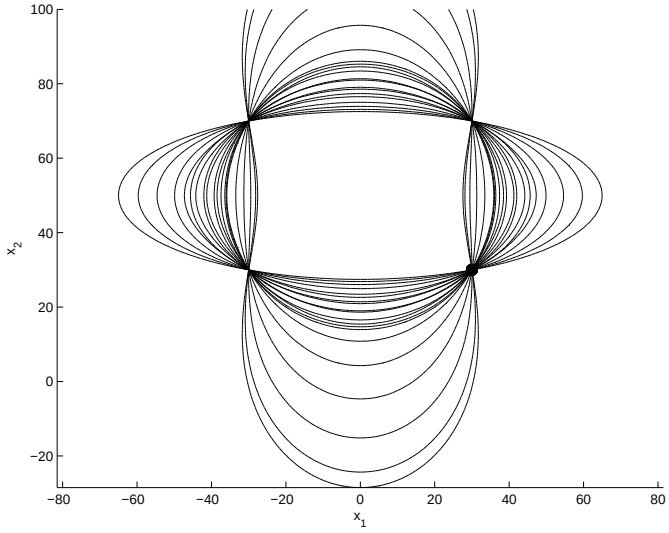

FIGURE 10. Figure shows intersections of the iso-range and iso-doppler contours of F_2 (or F_3) at the scatterer (30, 30) and at the artifact locations, in the same setting as in Fig 9.

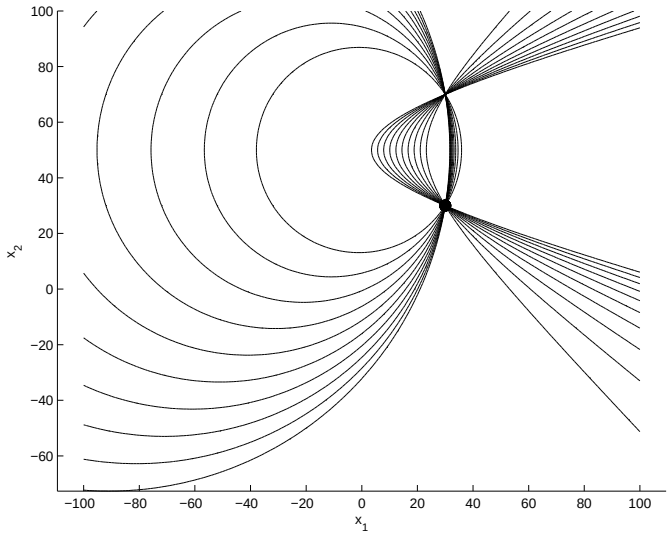

FIGURE 11. Figure shows intersections of the iso-range and iso-doppler contours of F_4 in the same setting as in Fig 9, 10.

[8] A. Grigis and J. Sjöstrand, "Microlocal Analysis for Differential Operators: an Introduction," London Mathematical Sciety Lecture Note Series, **196**, Cambridge University Press, 1994.
[9] G. T. Herman, H. K. Tuy, K. J. Langenberg and P. C. Sabatier, "Basic Methods of Tomography and Inverse Problems," Adam Hilger, Philadelphia, 1988.
[10] P. Morse and H. Feshbach, "Methods of Theoretical Physics," Vol. **1**, McGraw-Hill, 1953, MR:0059774.
[11] C. J. Nolan, *Scattering near a fold caustic*, SIAM J. of Appl. Math, **61** (2000), 659–672.

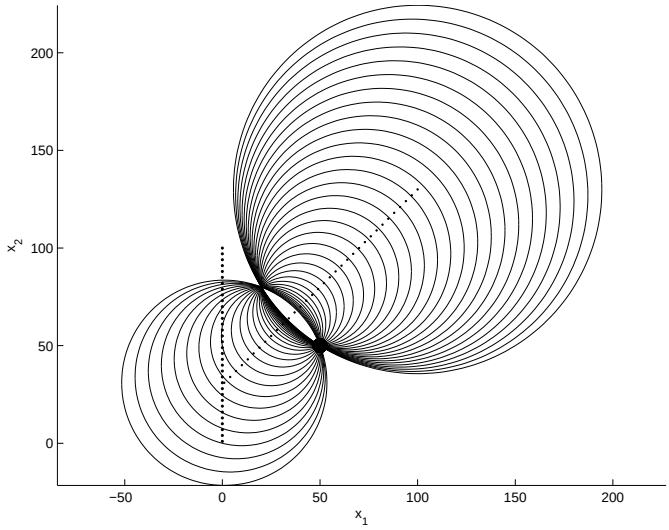

FIGURE 12. Picture showing the iso-range contours of F_1 in the case when the antenna is flying at a fixed height $h = 30$, on a straight line, making an angle of 45^0 from the perpendicular to the wall. The vertical line on the picture represents the wall, while the diagonal one represents the flight track. The spheres whose centres lie along the flight track intersect at the scatterer (50, 50) and at the artifact location.

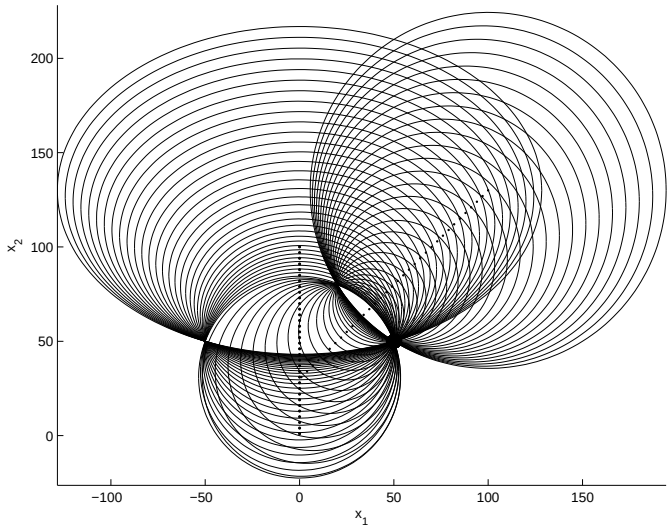

FIGURE 13. Picture showing the iso-range contours of F_1 and F_2 which contribute to the back-projection $F_1^\star \circ F_2$ (or $F_2^\star \circ F_1$) in the same situation described in previous figure.

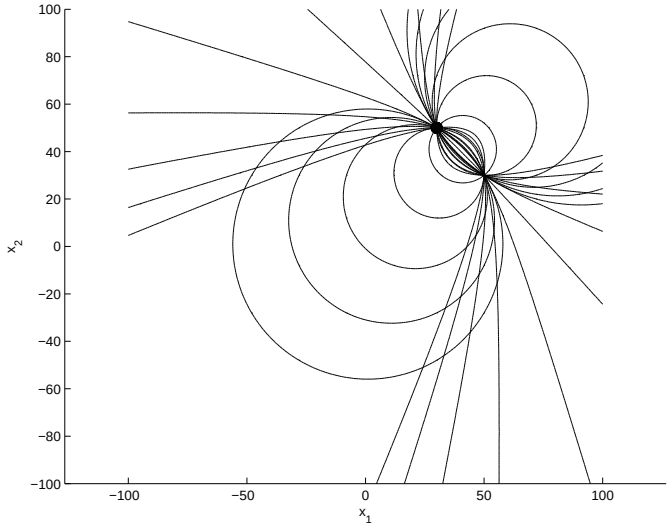

FIGURE 14. Figure shows intersections of the iso-range and iso-doppler contours of F_1 at the scatterer (30, 50) and at the artifact location, in the case when the antenna is flying on a straight line making an angle of 45^0 with the perpendicular to the wall, at the fixed height of $h = 25$. A similar picture can be found for F_4.

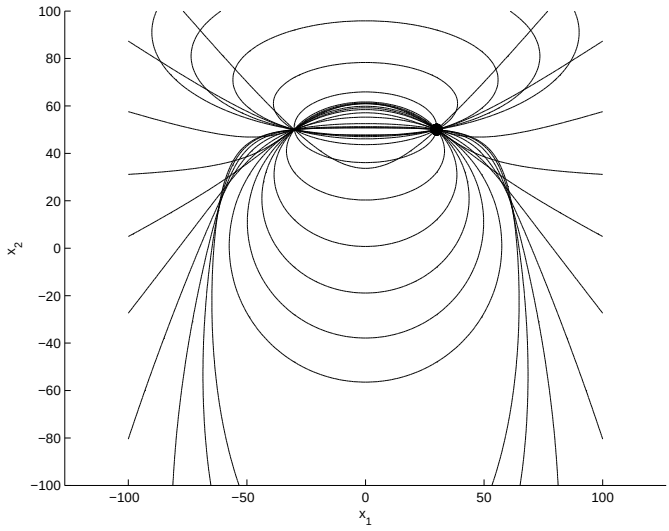

FIGURE 15. Figure shows intersections of the iso-range and iso-doppler contours of F_2 at the scatterer (30, 50) and at the artifact location, in the same situation as in previous figure.

[12] C. J. Nolan and M. Cheney, *Synthetic aperture inversion for arbitrary flight paths and non-flat topography*, IEEE Trans. on Image Processing, **12** (2003), no.9, 1035–1043, MR2006858.
[13] C. J. Nolan and M. Cheney, *Synthetic aperture inversion*, Inverse Problems, **18** (2002), no.1, 221–236, MR:1893592.

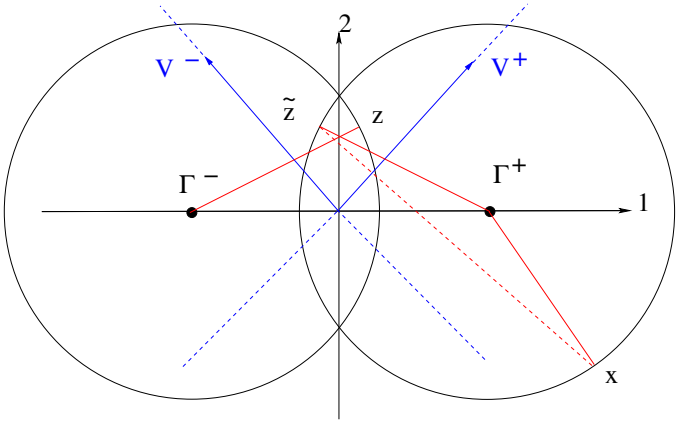

FIGURE 16. Figure shows that z-scatterer produces a σ_4 equal to σ_1 due to x-scatterer in experiment 1.

[14] C. J. Nolan and M. Cheney, *Microlocal analysis of synthetic aperture radar imaging*, J. Fourier Analysis and its Applications, **10** (2004), no.2, 133–148, MR:2054305.
[15] C. J. Nolan, M. Cheney, T. Dowling and R. Gaburro, *Enhanced angular resolution from multiply scattered waves*, Inverse Problems, **22** (2006), no.5, 1817–1834, MR:2261268.
[16] C. J. Nolan and W. W. Symes, *Global solution of a linearized inverse problem for the acoustic wave equation*, Comm. in PDE, **22**, (1997), no.5-6, 919–952, MR:1452173.
[17] M. Soumekh, *Bistatic synthetic aperture radar inversion with application in dynamic object imaging*, IEEE Trans. on Signal Processing, **39** (1991), 2044–2055.
[18] X. Saint Raymond, "Elementary Introduction to the Theory of Pseudodifferential Operators. Studies in Advanced Mathematics," CRC Press, Boca Raton, FL, 1991, MR:1211419.
[19] F. Treves, "Introduction to Pseudodifferential and Fourier Integral Operators," Vol. **I** and **II**, Plenum Press, New York-London, 1980, MR:0597145.
[20] L. M. H. Ulander and P. O. Frölund, *Ultra-wideband SAR interferometry*, IEEE Trans. Geosci. Remote Sensing, **36** (1998), 1540–1550.
[21] L. M. H. Ulander and H. Hellsten, *Low-frequency ultra-wideband array-antenna SAR for stationary and moving target imaging*, in Proce. Conf. SPIE 13th Annu. Int. Symp. Aerosense, Orlando, FL (1999).
[22] C. E. Yarman, B. Yazici and M. Cheney, *Bistatic synthetic aperture radar imaging for arbitrary flight trajectories*, submitted to IEEE-TIP, (2007).

Received September 2007; revised December 2007.

E-mail address: romina.gaburro@ul.ie
E-mail address: clifford.nolan@ul.ie